Journal of Inorganic and General Chemistry
ZAAC
Zeitschrift für anorganische und allgemeine Chemie

www.zaac.wiley-vch.de

ARTICLE

DOI: 10.1002/zaac.201500137

From Occupied Voids to Nanoprecipitates: Synthesis of Skutterudite Nanocomposites in situ

James Eilertsen,[a] Yuri Surace,[a] Sandor Balog,[b] Leyre Sagarna,[a] Gerda Rogl,[c] Jelena Horky,[d] Matthias Trottmann,[a] Peter Rogl,[c] M. A. Subramanian,[f] and Anke Weidenkaff*[e]

Dedicated to Professor Yuri Grin on the Occasion of His 60th Birthday

Keywords: Thermoelectric; Nanocomposite; Skutterudite; Nanoprecipitate; Nanoinclusion; Severe plastic deformation; High-pressure torsion

Abstract. Nanocomposite thermoelectrics can exhibit both reduced thermal conductivity and enhanced electrical conductivity beyond single-phase materials; accordingly, they have become the new material paradigm to achieve viable thermoelectric efficiencies. New synthesis techniques are needed to further enhance their properties. A novel technique, designed to synthesize nanoprecipitates within a well-sintered single-phase polycrystalline matrix, is reported. The technique, attrition-enhanced nanocomposite synthesis (AENS), comprises three stages: (1) Synthesis of cage-like crystal structures with metastable interstitials, followed by (2) severe plastic deformation (SPD), and finally (3) rapid sintering with concomitant interstitial precipitation. The efficacy of this technique is demonstrated in this work. Filled cage-like skutterudite $In_{0.2}Co_4Sb_{12}$ samples are synthesized and spark-plasma sintered. They are subjected to severe plastic deformation via high-pressure torsion, and finally sintered again via spark-plasma sintering in order to precipitate the metastable interstitials. X-ray diffraction, scanning-electron microscopy, and small-angle neutron scattering (SANS) of $In_{0.2}Co_4Sb_{12}$ samples subjected to this procedure demonstrate that indium precipitates rapidly, and forms nano-sized In-based inclusions. In addition, the amount of precipitated indium, and the size and distribution of the nanoprecipitates are strongly influenced by the extent of plastic deformation. This technique can be employed to synthesize efficient thermoelectrics as well as materials with a number of applications requiring rapid synthesis of nano-sized precipitates.

Introduction

Nanocomposites have exhibited enhanced material properties for centuries, the Bai-Lian and Damascus steels being legendary examples.[1,2] Nanocomposites, as described herein, are multiphase materials comprised of a micron-sized primary matrix phase with nano-sized secondary-phase inclusions. These nanoinclusions often enhance mechanical properties – such as, hardness, strength, and resistance to creep and fracture, and improve electrical and catalytic properties[3,4] – over their micron-scale composite and single-phase analogs. In addition, nanoinclusions are reported to significantly improve the efficiency of thermoelectric materials (TE)[5–7] – consequently, they have become the new *paradigm* for enhancing TE efficiencies.[8]

Further improvement of TE materials, particularly TE nanocomposites, is crucial to the implementation of sustainable energy solutions. Viable, high efficiency TE materials are one of many alternative energy technologies that may help to decelerate global climate change[9,10] as thermoelectric-based modules require only a thermal gradient to produce electric power, and do not emit greenhouse gases or other menacing pollutants. TE efficiency is derived from the electrical and thermal transport properties of the material. And is routinely quantified by the dimensionless Figure-of-merit (ZT): where $ZT = (S^2\sigma/\kappa_T)T$, where S is the Seebeck coefficient, σ the electrical conductivity, and κ_T is the total thermal conductivity measured at the operating temperature T. κ_T is comprised primarily of lattice (κ_L) and electronic (κ_e) components. κ_L is heat transported by crystal-lattice vibrations, phonons; and κ_e is heat transported

---

* Prof. Dr. A. Weidenkaff
E-Mail: weidenkaff@imw.uni-stuttgart.de
[a] Materials for Energy Conversion
Empa
Überlandstrasse 123
8600 Dübendorf, Switzerland
[b] Adolphe Merkle Institute
Université de Fribourg
Chemin des Verdiers 4
1700 Fribourg, Switzerland
[c] Institute for Physical Chemistry
Universität Wien
Währinger Straße 42
1090 Wien, Austria
[d] Physics of Nanostructured Materials
Universität Wien
Boltzmanngasse 5
1090 Wien, Austria
[e] Institut for Materials Science
Universität Stuttgart
Heisenbergstraße 3
70569 Stuttgart, Germany
[f] Department of Chemistry
Oregon State University
153 Gilbert Hall, Corvallis, OR 97331, USA

by charge carriers, proportionally related to the electrical conductivity (σ) by the Wiedemann-Franz relation. Accordingly, the reduction of phonon mean-free-path lengths (by scattering) and phonon velocity, and the enhancement (or maintenance) of electrical conductivity are essential strategies to further the development of viable TE materials.[8,11]

Current commercially available materials exhibit ZT's near 1, though this is too low for wide-scale energy applications.[12] TE nanocomposites, on the other hand, consistently surmount this barrier due to secondary, well-dispersed, nano-sized inclusions within a bulk primary-phase matrix. Nanoinclusions with dimensions smaller than the phonon mean-free path lengths scatter heat-carrying phonons, thus suppressing lattice thermal conductivity. However, for TE nanocomposites to be a viable and widely used technology further enhancement of the ZT via new synthesis techniques needs to be developed.

At present, nanocomposite thermoelectrics are synthesized by ball milling, precipitation, mixing, etc. However, TE materials with precipitated, segregated nanophases are thus far unsurpassed. Therefore, the ability to tune the precipitation kinetics, precipitate size and spatial distribution – to achieve optimal ZT-enhancing nanoinclusions – is essential in order to attain even higher ZT's. The yet undeveloped technique, attrition-enhanced nanocomposite synthesis (AENS), can achieve this aim.

First, AENS requires synthesis of open cage-like crystal structures that: (1) permit metastable substitutions and rapid diffusion of interstitials, and (2) possess high electrical conductivities and Seebeck coefficients – in effect, they must be relatively good *single-phase* thermoelectric materials. Skutterudites, with two large icosahedral voids per unit cell, and clathrates, with 8 and 24 polyhedral voids per unit cell in type I and type II, respectively; are ideal crystal structures for this technique (the former is investigated herein). Cobalt antimonide skutterudites, $CoSb_3$ or commonly Co_4Sb_{12}, have been researched for decades. Their large icosahedral voids can be filled with a wide range of elements that lower lattice thermal conductivity and improve electrical conductivity drastically.[13–16] The ZT for pristine $CoSb_3$ skutterudites, for example, can be enhanced from 0.051 ($T = 723$ K)[17] to ca. 1 with partial Yb filling[18] or indium filling[19–21] and 1.7 with multiple Ba, La, and Yb filling.[22] Further, a ZT ≈ 2 for (R,Ba,Yb)yCo_4Sb_{12}[23] following severe plastic deformation by high-pressure torsion has been reported. Moreover, they often exhibit good structural properties[13,24] and low coefficients of thermal expansion.[25–27] In addition, research focused on indium-filled skutterudites revealed that many samples contain ZT-enhancing InSb nanoinclusions formed in situ.[28–31] However, the source of indium has not yet been adequately established. The work of *Shi* et al.[22] theorized that in the skutterudite antimoides, void-site interstitials with electronegativities close to that of their antimony-based cages would not be stable. Consequently, the InSb nanoinclusion source-material was often ascribed to indium that was thermodynamically prohibited from entering the skutterudite crystal structure. The metastability of the indium-filled skutterudite crystal structure was later experimentally verified[25,32–34] providing conclusive evidence that the InSb nanoinclusions are synthesized with indium sourced *from* the defective metastably In-filled skutterudite voids. Accordingly, indium-filled skutterudites are particularly viable candidates for the first step of the AENS procedure.

Second, AENS requires the application of severe plastic deformation. In initial studies of the AENS technique,[32,33] it was reported that the amount of – plastic deformation incurred by indium-filled skutterduite samples – administered by ball milling – was directly related to the amount of indium that precipitated from the crystal structure upon further heating. This apparent boost in reaction kinetics is likely due to both (1) dislocation-enhanced precipitation – first proposed by *Cottrell*,[35] *Koehler*, and *Seitz*[36] – and the reduction of grain size.[37,38] Production of fine grain morphologies, dislocations, and other defects in polycrystalline materials can be achieved by more efficient techniques than ball milling, however. High-pressure torsion (HPT), a technique first proposed by *Bridgman* in the 1940's,[39] simultaneously applies Giga-Pascal pressures to a sample under rotation, ultimately producing submicron grain morphologies – often replete with dislocations – in a fraction of the time required by ball milling, and the technique eliminates the possibility of contamination by milling media.[40] In addition, HPT has been used extensively to precipitate well-dispersed nano-sized secondary phases in structural materials such as the Al-Fe,[41] Al-Cu,[42] Al-Li-Cu-Mg[43] alloys, and has been used extensively to generate sub-micron grain morphologies and dislocations in skutterudite materials.[44–47] Thus, HPT is ideal to enhance the precipitation kinetics of metastable fillers from cage-like thermoelectric materials – upon further heat treatment.

In fact, rapid heat treatment of the heavily deformed samples – to rapidly precipitate secondary inclusions and prevent their subsequent coarsening – is finally required. *Eilertsen* et al.[32] observed, by high-temperature X-ray diffraction, that maximal precipitation of indium from the skutterudite crystal structure occurred when deformed samples were heated to 600 °C at fast heating rates (100–200 $K \cdot min^{-1}$). Consequently, spark-plasma sintering is the ideal technique to obtain nano-sized secondary phases and relatively defect-free, fully sintered samples.

The efficacy of the aforementioned to the AENS process is investigated in this work. Analysis of samples produced after each stage of the process is conducted via X-ray diffraction, scanning-electron microscopy, and small-angle neutron scattering. Data from the samples at: *Stage 1*, as-synthesized, SPS'ed (Pre HPT); *Stage 2*, samples following HPT processing at room temperature (RT HPT) and 400 °C (HT HPT); and *Stage 3*, same samples following re-sintering via SPS (RT HPT SPS and HT HPT SPS) demonstrate that indium precipitates from $In_{0.2}Co_4Sb_{12}$ during re-sintering of both samples subjected to high-pressure torsion. The amount of precipitated indium, and the size and distribution of the nanoinclusions are influenced strongly by the degree of micro-structural deformation – varied here by processing temperature. Moreover, degradation of $CoSb_3$ to $CoSb_2$ and Sb is observed in the HPT-processed samples, though $CoSb_2$ and Sb re-react to form $CoSb_3$ during re-sintering.

Results and Discussion

1 Crystal Structure and Microstructure, Pre and Post HPT Processing

The as-synthesized Pre HPT sample was found to be pure phase via XRD. The sample is highly crystalline, and possesses a lattice parameter consistent with other reported indium-filled skutterudites[19,34] (Figure 1). Following HPT processing, a Sb-impurity phase was detected in the room temperature RT HPT samples, and a $CoSb_2$ impurity phase was detected in both RT HPT and high temperature HT HPT samples. Although some Sb-impurity phase is expected in the HT HPT sample, it is considered too small to be detected by laboratory XRD. In addition, the lattice parameters and crystallite strain increase, and the crystallite sizes decrease as compared to the as-synthesized Pre HPT sample. These effects are more pronounced in the room temperature (RT) processed sample as compared to the high-temperature (HT) processed sample (Table 1).

Specifically, following HPT processing, the lattice-parameter increases 0.06 % and 0.02 % in the RT HPT and HT HPT samples, respectively. The strain is more than four times greater in the RT HPT sample than the as-synthesized Pre HPT sample, while the strain in the HT HPT sample is relatively unchanged – probably due to annealing during the HT processing. Although the crystallite sizes are nearly halved by HPT processing, they are nearly the same for both RT HPT and HT HPT samples; their magnitudes are consistent with previous studies.[48]

The microstructures of the Pre HPT, RT HPT, and HT HPT samples are shown in Figure 2. The Pre HPT sample is well sintered; the grains are micron-sized. The sample microstructure is completely transformed following HPT processing. HPT processing produces nano-sized grains and significant structural damage (Figure 2b,c). Both room-temperature and high-temperature samples exhibited numerous cracks, that severely complicate reliable electrical and thermal transport property characterizations. The high-temperature HPT sample exhibited a systematic network of radial cracks near the edge of the sample (Figure 2d–f).

The difference in crystallite strain in the RT HPT and HT HPT samples is due to temperature-dependent defect formation. Since appreciable dislocation formation in $CoSb_3$ crystallites is not likely above $0.3Td$ (Td: peritectic decomposition T) and the Td of $CoSb_3$ is 876 °C, few crystallite-strain-dominating dislocations are produced in the HT-processed sample, while they are replete in the RT-processed sample. The observed lattice-parameter expansion and $CoSb_2$ formation are due to antimony self-insertion, as previously reported[49–51] and the subsequent collapse of the $CoSb_3$ phase under Giga-Pascal pressures. As above, the effect is more pronounced in the RT-processed sample as compared to the HT-processed sample as (1) the strain energy (attendant with dislocations) is

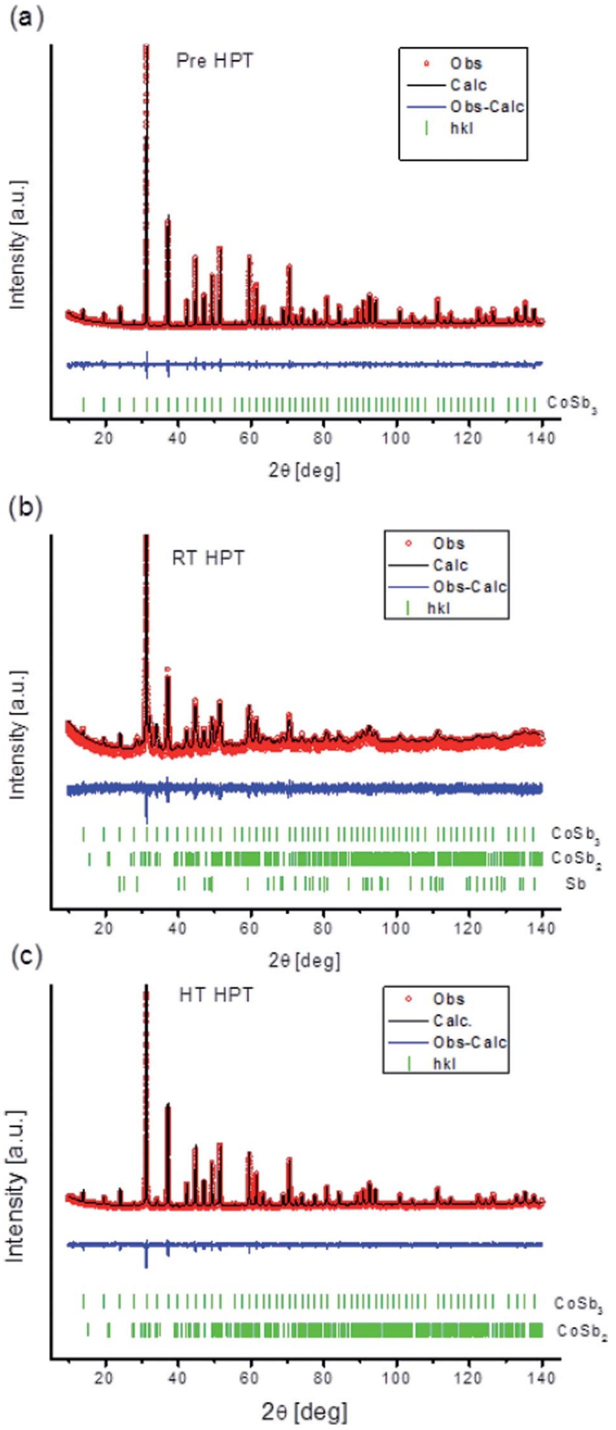

Figure 1. XRD Data and Le Bail Whole-Profile Fitting of $In_{0.2}Co_4Sb_{12}$ (a) as-synthesized, (b) following room-temperature HPT, and (c) high-temperature HPT processing. Calculated reflections corresponding to the $CoSb_3$ /Co_4Sb_{12}, $CoSb_2$, and Sb are shown. The as-synthesized Pre HPT sample (a) is pure phase, while an Sb impurity is detected in the RT HPT sample, and a $CoSb_2$ impurity is detected in both the RT HPT and HT HPT samples. HPT increases the lattice parameter of both (b) and (c).

higher in the RT sample; and (2) Sb de-insertion occurs at temperatures greater than 180 °C (at ambient pressure) as reported by *Miotto* et al.[50] Hence Sb de-insertion, nucleation,

Table 1. Lattice parameters of the samples.

Samples	R_p	R_{wp}	R_{exp}	χ^2	a /Å	Size /Å	Error	Strain	Error
Pre HTP	5.82	7.47	6.27	1.42	9.04559	768.69	0.94	8.3618	0.0048
RT HTP	5.37	6,78	5.8	1.36	9.05105	478.79	0.38	34.3662	0.0366
HT HPT	5.26	7.00	5.59	1.57	9.04498	459.26	2.37	8.4051	0.0078
RT Post SPS	5.33	6.92	5.93	1.36	9.04181	923.83	1.48	12.2223	0.0259
HT Post SPS	4.99	6.37	5.61	1.29	9.04705	1268.94	0.33	2.0437	0.003

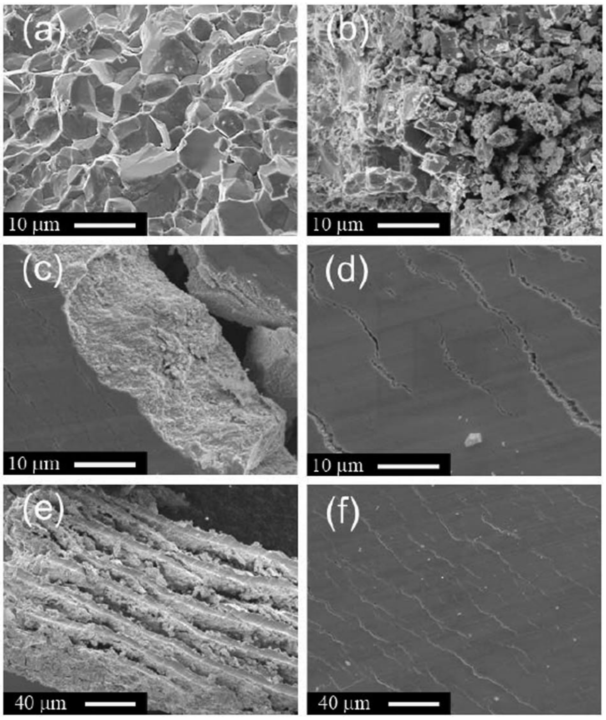

Figure 2. SEM of Pre HPT (a), RT HPT (b), and HT HPT (c–f). The grains are well sintered in the Pre HPT sample (a); following HPT processing the sample grains are severely transformed (b, c) to sub-micron grains/particles. A systematic network of radial cracks well distributed in the outer radius of the sample.

and growth occur upon cooling the HT sample from 400 °C to room temperature. This effect is supported by SEM (Figure 3). The microstructure of the HT HPT sample is shown. Systematic micro-cracks are present, and are especially prevalent near the edges of the HT HPT-processed sample. The micro-cracks, as well as other defects, act as powerful centers for the nucleation of Sb precipitated from the skutterudite crystal structure. The subsequent micron-sized Sb crystals, confirmed by EDX, are distributed near the edges of the sample. Although, an Sb-impurity phase was detected via XRD, no Sb precipitates were detected by SEM in the room-temperature processed sample since the Sb in the RT-processed sample lacked sufficient thermal energy to form micron-sized crystals as seen in the HT HPT sample.

2 Crystal Structure and Microstructure, Post SPS re-sintering

SPS-processing, in effect, acts as a brief 600 °C, 20-minute anneal or heat treatment. Consequently, the $CoSb_2$ and Sb impurity phases are no longer detected by XRD (Figure 4). As *Biswas* et al. demonstrated,[52] synthesis of $CoSb_3$ in a few minutes is possible. Moreover, the crystallite sizes increase and the strain decreases significantly in both samples (Table 1). In addition, a lattice-parameter contraction is observed in both samples following SPS re-sintering. The resultant lattice parameters of both RT HPT and HT HPT samples following SPS re-sintering are less than the original Pre HPT sample. Therefore, the observed contraction is profound evidence for the precipitation of both Sb and indium from the skutterudite crystal structure. As the lattice-parameter contraction is greater in the RT-processed sample, precipitation from the skutterduite crystal is judged to be strongly dependent on the amount of structural defects present in the sample prior to the final SPS re-sintering (heat treatment) consistent with findings reported before.[32]

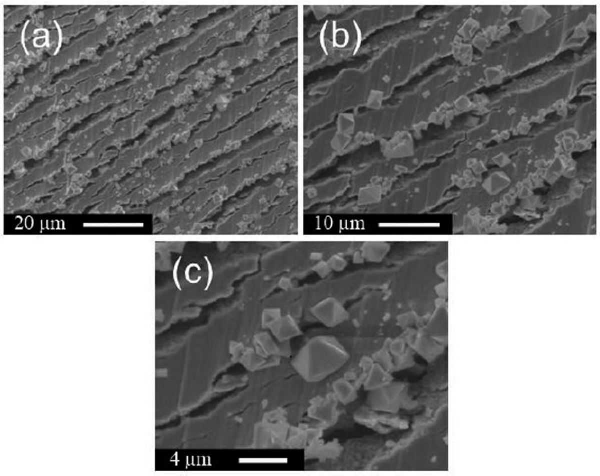

Figure 3. SEM of the HT HPT sample (a–c). The network of radial cracks near the outer radius of the sample likely assisted the nucleation and growth of Sb single crystals during HPT processing at 400 °C – likely upon cooling. The composition of the Sb single crystals was confirmed by EDX. Note, the Sb single crystals were largely concentrated near the outer edge of the HT HPT sample, and are not detected via XRD.

SEM analysis of the precipitates morphology in the Pre HPT, RT HPT, and HT HPT samples following SPS re-sintering, are shown (Figure 5). All samples, even the Pre HPT sample subjected to no structural disturbance, precipitate nano-sized phases. The precipitates in the Pre HPT sample, however, were observed to be very poorly dispersed and were larger (ca. 100 nm) than the HT HPT-processed sample (ca. 30 nm). In addition, these precipitates were only found in a few select regions. The nanoprecipitates spatial distribution (depicted in Figure 5a) is not representative of the sample as a whole.

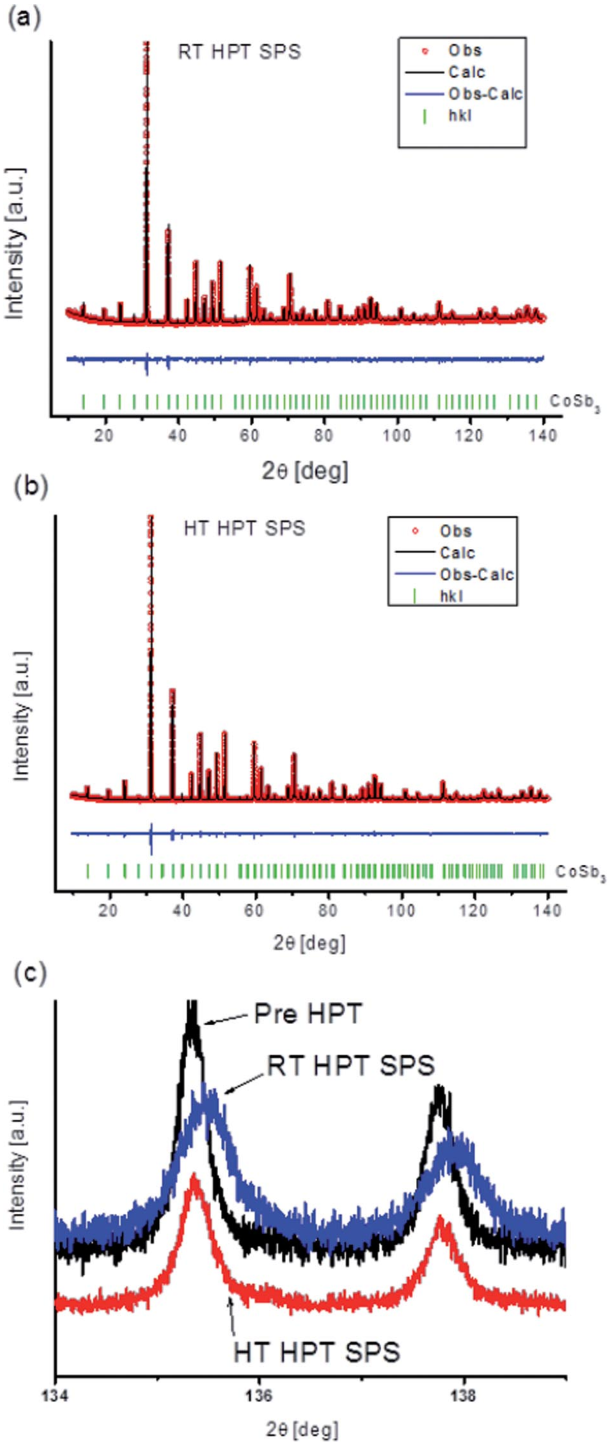

Figure 4. XRD Data and Le Bail Whole-Profile Fitting of HPT-processed In0.2Co4Sb$_{12}$ samples following SPS re-sintering. No impurity phases are detected in the room temperature (a) and 400 °C (b) HPT-processed samples following SPS re-sintering (rapid heat treatment). Le Bail Whole-Profile Fittings reveal a small lattice parameter contraction occurred upon re-sintering for the HT HPT sample as compared to the as-synthesized Pre HPT sample, and a large contraction for the re-sintered RT HPT sample. A corresponding shift to higher angles (2θ) is also readily apparent for the RT HPT SPS sample (c). Note, the $CoSb_2$ and Sb impurity phases are no longer detected (a and b) following SPS re-sintering.

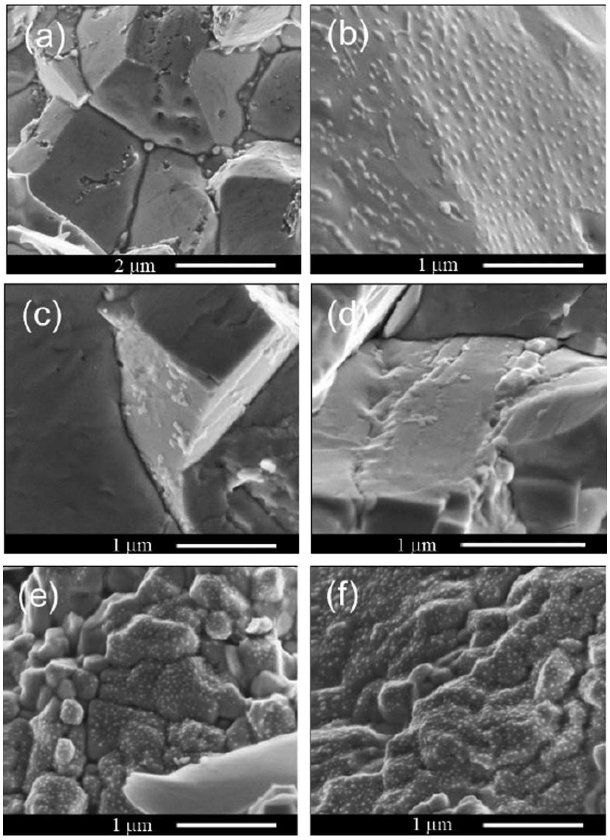

Figure 5. Morphology, size, and distribution of the nanoprecipitates in Pre HPT (a, b), RT HPT SPS (c, d), and HT HPT SPS (e, f). The nanoprecipitates are poorly distributed in the Pre HPT sample. Many regions (a) are without precipitates, some grains exhibit a high concentration of ca. 100 nm precipitates. The precipitates in the RT-processed sample are strongly coalesced with dimensions >100 nm, while the precipitates in the HT-processed sample are well dispersed, with diameters of about 30 nm.

Conversely, the HPT-processed, re-sintered samples show enhanced nanoprecipitate spatial distribution (Figure 5c–f). Nearly every region in both HPT-processed samples possesses nanoprecipitates. Nevertheless, a marked difference in nanoprecipitate morphology between the RT- and HT-processed samples is readily apparent. The nanoprecipitates in the RT sample are coarse and largely coalesced (>100 nm). The nanoprecipitates in the HT sample, however, exhibit better spatial distribution and are quite small in comparison (ca. 30 nm). The difference in nanoprecipitate morphology is due to the difference in structural distortion. As disturbance increases, the energy threshold for precipitation decreases; thereby resulting in rapidly precipitated and ultimately coalesced precipitates in the RT-processed sample, consistent with previous studies.[32] Consequently, better spatial distribution and smaller precipitate sizes are found in the HT-processed sample as it was subjected to milder plastic deformation.

Small-angle neutron scattering (SANS) analysis conducted on all samples, supports the aforementioned (Figure 6). The PRE HPT sample displays the lowest scattering intensity, while the overall scattering intensity increases significantly after HPT treatment. The observed increase is greater in the RT

HPT sample than the HT HPT sample. The increase in the scattering intensity is due to the genesis of nano-sized grains during HPT processing. Nano-sized grains in the pure-phase HPT processed samples increases the overall surface to volume ratio, which contributes to the increased scattering intensity considerably.[53] The difference in scattering intensity between the RT HPT and HT HPT samples indicates there are more nano-sized particles / grains in the RT HPT sample. Although crystallite sizes derived from Le Bail Whole-Profile Fittings indicate the crystallite sizes are nearly the same in both RT HPT and HT HPT samples, a large number of amorphous, nano-sized particles likely occur in the RT HPT processed sample, thus contributing to the higher scattering intensity. Subsequent heat treatment of the HPT-processed samples (RT HPT SPS and HT HPT SPS) increases the typical size of the matrix grains, but also promotes the formation of nano-sized precipitates/indium-based inclusions.

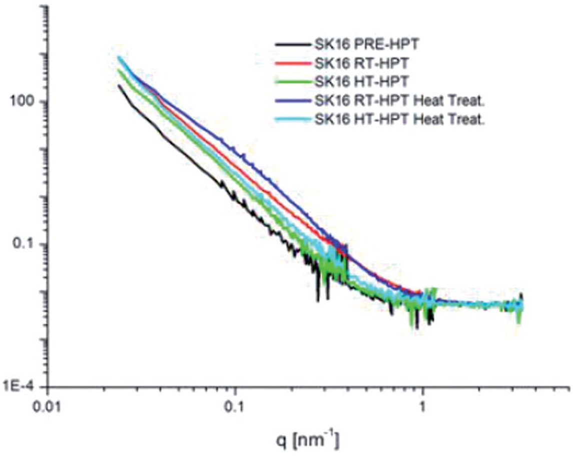

Figure 6. SANS data of all samples. The scattering intensity increases in the RT HPT and HT HPT samples due to the formation of nano-sized matrix grains. The scattering intensity due to the matrix grains decreases after SPS re-sintering (RT HPT SPS, HT HPT SPS) as the grains grow. However scattering increases in the same sample due to the presence of indium-based nanoprecipitates in the samples following SPS re-sintering. Note, the scattering intensity in the Pre HPT samples is less than both RT HPT SPS and HT SPS samples due to the presence of nanoprecipitates in the latter two samples.

Assuming a biphasic system (matrix + precipitates) in the Pre HPT, RT HPT SPS, and HT HPT SPS samples, the overall volume fraction of precipitated indium can be estimated via the scattering invariant defined by Q = dq q2Iq $\propto$f(1–f), where f is the volume fraction of the precipitated phase. When f $<<$ 1, Q is simply proportional to f. Accordingly, the overall volume fraction of the precipitated indium increases by approximately 40 % (RT HPT SPS) and 50 % (HT HPT SPS) due to SPS re-sintering heat treatment. Although the observed lattice parameter contraction, and concomitant indium precipitation – derived from XRD was far greater in the RT HPT SPS sample as compared to the HT HPT SPS sample. The SANS scattering intensity is lower because much of the indium coalesces as $>$100 nm sized precipitates, whereas the precipitates in the HT HPT SPS sample are well distributed, and far smaller, ca. 30 nm, thereby resulting in a scattering intensity that is greater than the RT HPT SPS sample.

Conclusions

X-ray diffraction, scanning-electron microscopy, and small-angle neutron scattering were used to evaluate the efficacy of the attrition-enhanced nanocomposite synthesis (AENS) technique designed to produce nanoprecipitates from highly defective metastably indium-filled $In_{0.2}Co_4Sb_{12}$ skutterudites. High-pressure torsion (HPT) was used to stimulate precipitation of indium from the skutterudite void sites. HPT produced the greatest crystallite strain in a sample subjected to HPT at room temperature. Accordingly, this sample precipitated the largest amount of indium upon re-sintering. The smallest nanoprecipitates with the best spatial distribution, however, were found in the HPT sample processed at high temperature. This study, therefore, demonstrates the strong correlation between structural defects, namely dislocations, on the precipitation kinetics in filled skutterudites, and is applicable to numerous cage-like crystals systems with metastable interstitials.

Experimental Section

1 Attrition-enhanced Nanocomposite Synthesis (AENS Synthesis)

A 10-gram batch of indium-filled $In_{0.2}Co_4Sb_{12}$ was synthesized from elemental indium (Aldrich, 100 mesh, 99.99 %), cobalt (Aldrich, $<$ 2 um, 99.8 %), and antimony (Alfa Aesar, 100 mesh, 99.5 %). The powders were mixed and pressed into a pellet. The pellet was loaded into a quartz tube, sealed under vacuum, and heated according to the procedure developed by *He* et al.[19] The synthesized pellet was pulverized in an agate mortar, transferred into a graphite-foil-lined, 12 mm-graphite die and loaded into a spark plasma sintering system from FCT Syteme GmbH. The samples were purged with argon and heated to 600 °C under vacuum with a heating ramp rate of 100 $K\cdot min^{-1}$, sintered in DC mode using 15 ms / 2 ms (pulse / rest) and 6 kN of applied force. The sample chamber was rapidly cooled to room temperature at approximately 100 $K\cdot min^{-1}$, and finally back-filled with argon. The as-sintered pellet achieved nearly 100 % the theoretical density. The sintered pellet was cut into nearly 1.1-mm thick discs and finally ground and polished to 10 mm diameter and 1 mm thick discs for HPT experiments. During HPT, the discs were subjected to 4 GPa of pressure, and rotated once at a rotation speed of 0.2 rotations per min. HPT processing was performed at both room temperature and at 400 °C. Following HPT processing the samples were re-sintered via SPS (crushed to powders or inserted as discs in order to precipitate indium from the skutterudite crystal structure and eliminate excessive structural defects, e.g. dislocations, from the microstructure.

2 Crystal Structure Characterization

Powder X-ray diffraction (XRD) data were collected on sintered samples before and after HPT processing with a PANalytical X'Pert PRO θ-2θ scan system equipped with Johansson monochromator and the ultra-fast X'Celerator linear detector. The diffraction patterns were collected with a scan rate from 10° to 140° (2θ) at $0.004830°\cdot s^{-1}$. The samples were loaded onto an oriented Si single-crystal sample holder with near-zero back-ground to maximize the possibility of detecting impurity phases. The diffraction data were analyzed using the Le Bail technique[54,55] as implemented in the Fullprof program. Peak shape was described by a Thompson-Cox-Hastings pseudo-Voigt function with asymmetric parameters for low-angle domain peaks (below 40° 2θ).

3 Microstructural Characterization

The morphology of the Pre HPT, RT HPT, and HT HPT samples was studied by scanning electron microscopy (SEM) with an XL30 ESEM (FEI Company) operating at 10 kV with a secondary electron (SE) detector. The samples were placed each on an aluminum SEM holder with a carbon double side adhesive disk. The composition was analyzed by energy dispersive X-ray spectroscopy (EDX) with an EDAX detecting unit (EDAX Inc). In addition, the morphologies of the Pre HPT, RT HPT SPS, and HT HPT SPS samples were investigated with a Scanning Electron Microscope (SEM) FEI Nova NanoSEM 230 using ETD (Everhart-Thornley) and TLD (Through-Lens) detectors with electron-beam energy of 5 keV.

In addition, SANS experiments of all samples were performed at the Swiss spallation neutron source SINQ (Paul Scherrer Institute at Villigen, Switzerland) using the SANS-I beam-line. Measurements were carried out using three different scattering geometries: sample-to-detector distance of 2, 6, and 18, m with neutron wave-length of 0.6 nm. Raw data were processed according to standard procedures and were calibrated for detector nonlinearity using the incoherent scattering from water. Scattering was isotropic, and thus, we present azimuthally integrated scattering spectra as a function of momentum transfer, $q = 4\pi\cdot\lambda–1\cdot\sin(\theta/2)$, where θ is the scattering angle and λ is the neutron wavelength.

Acknowledgements

This research was supported by a Marie Curie Fellowship (PCOFUND-GA-2010–267161) and by the Deutsche Forschungsgemeinschaft Priority Program SPP 1386. The authors thank Prof. *Dr. Michael Zehetbauer* (University of Vienna, Institute for Physical Chemistry, Austria) for access to the high-pressure torsion equipment, and *Dr. Joachim Kohlbrecher* (Paul Scherrer Institute, Switzerland) for conducting the SANS experiments at the SINQ neutron source.

References

[1] T. G. Langdon, in: *Materials Science Forum. Nanomaterials by Severe Plastic Deformation: NanoSPD5* (Eds.: J. T. Wang, R. B. Figueiredo, T. G. Langdon), Trans. Tech Publications Inc., Pfäffikon, **2010**.
[2] M. Reibold, P. Paufler, A. A. Levin, W. Kochmann, N. Pätzke, D. C. Meyer, *Nature* **2006**, *444*, 286.
[3] M. Sternitzke, *J. Eur. Ceram. Soc.* **1997**, *17*, 1061–1082.
[4] S. Komarneni, *J. Mater. Chem.* **1992**, *2*, 1219.
[5] A. J. Minnich, M. S. Dresselhaus, Z. F. Ren, G. Chen, *Energy Environ. Sci.* **2009**, *2*, 466.
[6] A. J. Minnich, G. Chen, *Appl. Phys. Lett.* **2007**, *91*, 073105.
[7] M. Martín-González, O. Caballero-Calero, P. Díaz-Chao, *Renewable Sustainable Energy Rev.* **2013**, *24*, 288–305.
[8] M. G. Kanatzidis, *Chem. Mater.* **2010**, *22*, 648–659; K. F. Hsu, S. Loo, F. Guo, W. Chen, J. S. Dyck, C. Uher, T. Hogan, E. K. Polychroniadis, M. G. Kanatzidis, *Science* **2004**, *303*, 818; W. Liu, Z. Ren, G. Chen, *Nanostructured Thermoelectric Materials*, in *Thermoelectric Nanomaterials*, (Eds.: K. Koumoto, T. Mori), Springer, Heidelberg, **2013**, pp. 255–286.
[9] T. M. Tritt, M. A. Subramanian, *MRS Bull.* **2006**, *31*, 188–198.
[10] G. J. Snyder, E. S. Toberer, *Nat. Mater.* **2008**, *7*, 105–114.
[11] G. Chen, M. S. Dresselhaus, G. Dresselhaus, J.-P. Fleurial, T. Caillat, *Int. Mater. Rev.* **2003**, *48*, 45–66.
[12] L. E. Bell, *Science* **2008**, *321*, 1457–1461.
[13] B. C. Sales, D. Mandrus, R. K. Williams, *Science* **1996**, *272*, 1325–1328.
[14] B. Sales, D. Mandrus, B. Chakoumakos, V. Keppens, J. Thompson, *Phys. Rev. B* **1997**, *56*, 15081–15089.
[15] G. S. Nolas, D. T. Morelli, T. M. Tritt, *Annu. Rev. Mater. Sci.* **1999**, *29*, 89–116.
[16] G. Nolas, J. Cohn, G. Slack, *Phys. Rev. B* **1998**, *58*, 164–170.
[17] Y. Kawaharada, K. Kurosaki, M. Uno, S. Yamanaka, *J. Alloys Compd.* **2001**, *315*, 193–197.
[18] G. S. Nolas, M. Kaeser, R. T. Littleton, T. M. Tritt, *Appl. Phys. Lett.* **2000**, *77*, 1855.
[19] T. He, J. Chen, H. D. Rosenfeld, M. A. Subramanian, *Chem. Mater.* **2006**, *18*, 759–762.
[20] A. Sesselmann, T. Dasgupta, K. Kelm, E. Müller, S. Perlt, S. Zastrow, *J. Mater. Res.* **2011**, *26*, 1820–1826.
[21] R. C. Mallik, *Met. Mater. Int.* **2008**, *14*, 223–228.
[22] X. Shi, J. Yang, J. R. Salvador, M. Chi, J. Y. Cho, H. Wang, S. Bai, J. Yang, W. Zhang, L. Chen, *J. Am. Chem. Soc.* **2011**, *133*, 7837–7846; J. Y. Peng, P. N. Alboni, J. He, B. Zhang, Z. Su, T. Holgate, N. Gothard, T. M. Tritt, *J. Appl. Phys.* **2008**, 104, 053710.
[23] G. Rogl, A. Grytsiv, P. Rogl, N. Peranio, E. Bauer, M. Zehetbauer, O. Eibl, *Acta Materialia* **2014**, *63*, 30–43.
[24] G. Rogl, P. Rogl, *Sci. Adv. Mater.* **2011**, *3*, 517–538.
[25] J. Eilertsen, R. Berthelot, A. W. Sleight, M. A. Subramanian, *J. Solid State Chem.* **2012**, *190*, 238–245.
[26] T. Caillat, A. Borshchevsky, J.-P. Fleurial, *J. Appl. Phys.* **1996**, *80*, 4442.
[27] G. Rogl, L. Zhang, P. Rogl, A. Grytsiv, M. Falmbigl, D. Rajs, M. Kriegisch, H. Müller, E. Bauer, J. Koppensteiner, *J. Appl. Phys.* **2010**, *107*, 043507.
[28] S. Ballikaya, G. Wang, K. Sun, C. Uher, *J. Electron. Mater.* **2011**, *40*, 570–576.
[29] J. Graff, S. Zhu, T. Holgate, J. Peng, J. He, T. M. Tritt, *J. Electron. Mater.* **2011**, *40*, 696–701.
[30] H. Li, X. Tang, Q. Zhang, C. Uher, *Appl. Phys. Lett.* **2009**, *94*, 102114.
[31] R. C. Mallik, C. Stiewe, G. Karpinski, R. Hassdorf, E. Müller, *J. Electron. Mater.* **2009**, *38*, 1337–1343.
[32] J. Eilertsen, S. Rouvimov, M. A. Subramanian, *Acta Materialia* **2012**, *60*, 2178–2185.
[33] J. Eilertsen, M. Trottmann, S. Populoh, R. Berthelot, C. M. Cooke, M. K. Cinibulk, S. Pokrant, A. Weidenkaff, M. A. Subramanian, *MRS Online Proc. Libr.* **2013**, *1490*, 27–32.
[34] A. Grytsiv, P. Rogl, H. Michor, E. Bauer, G. Giester, *J. Electron. Mater.* **2013**, *42*, 2940–2952.
[35] *Effect of Solute Atoms on the Behaviour of Dislocations* (Ed.: A. H. Cottrell), Report on Conference, **1948**.
[36] J. S. Köhler, F. Seitz, *J. Appl. Mech. Trans. ASME* **1947**, *14*, A217-A224.
[37] F. R. Nabarro, *Dislocations in Solids*, *The Elastic Theory*, vol. 1, North-Holland Publ., Amsterdam, **1979**.
[38] M. A. Tschopp, K. N. Solanki, F. Gao, X. Sun, M. A. Khaleel, M. F. Horstemeyer, *Phys. Rev. B* **2012**, *85*.
[39] P. W. Bridgman, *J. Appl. Phys.* **1943**, *14*, 273.
[40] A. Zhilyaev, T. Langdon, *Prog. Mater. Sci.* **2008**, *53*, 893–979.
[41] O. N. Senkov, F. H. Froes, V. V. Stolyarov, R. Z. Valiev, J. Liu, *Nanostruct. Mater.* **1998**, *10*, 691–698.
[42] Y. Huang, J. D. Robson, P. B. Prangnell, *Acta Materialia* **2010**, *58*, 1643–1657.
[43] S. Lee, Z. Horita, S. Hirosawa, K. Matsuda, *Mater. Sci. Eng. A* **2012**, *546*, 82–89.
[44] G. Rogl, D. Setman, E. Schafler, J. Horky, M. Kerber, M. Zehetbauer, M. Falmbigl, P. Rogl, E. Bauer, in: *NATO Science for*

Peace and Security Series. Series B, Physics and Biophysics (Eds.: V. Zlatić, A. C. Hewson), Springer, Dordrecht, **2013**.
[45] G. Rogl, Z. Aabdin, E. Schafler, J. Horky, D. Setman, M. Zehetbauer, M. Kriegisch, O. Eibl, A. Grytsiv, E. Bauer, *J. Alloys Compd.* **2012**, *537*, 183–189.
[46] G. Rogl, A. Grytsiv, E. Royanian, P. Heinrich, E. Bauer, P. Rogl, M. Zehetbauer, S. Puchegger, M. Reinecker, W. Schranz, *Acta Materialia* **2013**, *61*, 4066–4079.
[47] G. Rogl, A. Grytsiv, M. Falmbigl, E. Bauer, P. Rogl, M. Zehetbauer, Y. Gelbstein, *J. Alloys Compd.* **2012**, *537*, 242–249.
[48] G. Rogl, P. Rogl, E. Bauer, M. Zehetbauer, in: *Thermoelectric Nanomaterials*. *Materials Design and Applications* (Eds.: K. Kōmoto, T. Mori), Springer, Berlin, New York, **2013**.
[49] K. Matsui, J. Hayashi, K. Akahira, K. Ito, K. Takeda, C. Sekine, *J. Phys.: Conf. Ser.* **2010**, *215*, 012005.
[50] F. Miotto, C. A. Figueirêdo, G. R. Ramos, C. L. G. Amorim, M. R. Gallas, C. A. Perottoni, *J. Appl. Phys.* **2011**, *110*, 043529.
[51] K. Matsui, K. Yamamoto, T. Kawaai, Y. Kawamura, J. Hayashi, K. Takeda, C. Sekine, *J. Phys. Soc. Jpn.* **2012**, *81*, 104604.
[52] K. Biswas, S. Muir, M. A. Subramanian, *Mater. Res. Bull.* **2011**, *46*, 2288–2290.
[53] A. Guinier, G. Fournet, *Small-angle Scattering of X-rays*, Wiley & Sons, New York, **1955**.
[54] A. Le Bail, H. Duroy, J. L. Fourquet, *Mater. Res. Bull.* **1988**, *23*, 447–452.
[55] J. Rodríguez-Carvajal, *Phys. B: Condens. Matter* **1993**, *192*, 55–69.

Received: March 9, 2015